

Improved Algorithms and Coupled Neutron-Photon Transport for Auto-Importance Sampling Method *

Xin Wang(王鑫)^{1,2} Zhen Wu(武祯)³ Rui Qiu(邱睿)^{1,2;1)} Chun-Yan Li(李春艳)³
Man-Chun Liang(梁漫春)¹ Hui Zhang(张辉)^{1,2} Jun-Li Li(李君利)^{1,2}

¹Department of Engineering Physics, Tsinghua University, Beijing 100084, China

²Key Laboratory of Particle & Radiation Imaging, Ministry of Education, Beijing 100084, China

³Nuctech Company Limited, Beijing 100084, China

Abstract: The Auto-Importance Sampling (AIS) method is a Monte Carlo variance reduction technique proposed for deep penetration problems, which can significantly improve computational efficiency without pre-calculations for importance distribution. However, the AIS method is only validated with several simple examples, and cannot be used for coupled neutron-photon transport. This paper presents the improved algorithms for the AIS method, including particle transport, fictitious particles creation and adjustment, fictitious surface geometry, random number allocation and calculation of the estimated relative error. These improvements allow the AIS method to be applicable to complicated deep penetration problems with complex geometry and multiple materials. A coupled Neutron-Photon Auto-Importance Sampling (NP-AIS) method is proposed to solve the deep penetration problems of coupled neutron-photon transport using the improved algorithms. The NUREG/CR-6115 PWR benchmark was calculated by using the methods of NP-AIS, geometry splitting with Russian roulette and the analog Monte Carlo, respectively. The calculation results of NP-AIS were in good agreement with those of geometry splitting with Russian roulette and the benchmark solutions. The computational efficiency of NP-AIS for both neutron and photon was much better than that of geometry splitting with Russian roulette in most cases, and increased by several orders of magnitude compared with that of the analog Monte Carlo.

Key words: Monte Carlo, deep penetration, auto-importance sampling, coupled neutron-photon transport

PACS: 24.10.Lx

1 Introduction

To solve deep penetration problems in radiation shielding calculation using Monte Carlo (MC) simulation, many methods have been developed based on the theory of coupling with deterministic method. These methods include different types of Monte Carlo variance reduction techniques [1,2,3,4] and coupled MC/discrete-ordinates method[5,6,7]. However, these solutions have some limitations. The most effective Monte Carlo variance reduction techniques for deep penetration problems, for instance, importance sampling and geometry splitting with Russian roulette, require experience and pre-calculations for importance distribution, which are very time-consuming. Coupled MC/discrete-ordinates method must determine the interface position and convert the data structure between MC and discrete-ordinates simulations.

MC and discrete-ordinates methods may be switched many times in some complicated deep penetration problems.

The Auto-Importance Sampling (AIS) method [8,9] is a new Monte Carlo variance reduction technique proposed by Tsinghua University for deep penetration problems, which can automatically adjust the particle importance distribution while transporting particles in layered space continuously. In general, the AIS method divides the whole geometry space into $K+1$ sub-spaces by introducing K fictitious surfaces; particles are transported in these sub-spaces in sequence. The fictitious surface k ($k=1,2,\dots,K$) is the Current Fictitious Surface (CFS) of sub-space k . In each sub-space, except for the last sub-space, fictitious particles are created on CFS using next event estimator while transporting source particles and secondary particles. The source particles and secondary particles will be killed

* Supported by the subject of National Science and Technology Major Project of China (2013ZX06002001-007) and National Natural Science Foundation of China (11275110, 11375103)

1) E-mail: qiurui@tsinghua.edu.cn

if they traverse CFS. After all the source particles are simulated, the weights and number of fictitious particles are automatically adjusted using splitting/Russian roulette method until the number of fictitious particles are adjusted to be as many as the source particles. Then, the fictitious particles are set as the source of the next sub-space, and the particle transport is performed in the next sub-space. More detailed information about the AIS method can be found in Ref. [8].

Currently, the AIS method is implemented in MCNP5 [10] code, and can be applied to neutron or photon transport, separately. Compared with the analog Monte Carlo, the computational efficiency of the AIS method is increased by about three orders of magnitude for several simple deep penetration problems. However, coupled neutron-photon transport calculations must be considered for some typical deep penetration problems in engineering, for instance, shielding calculations for reactors and high energy accelerators. Aside from this, the application of the AIS method is limited due to the following disadvantages:

- 1) The particles traversing CFS during transport in each sub-space will affect the tally results around CFS.
- 2) Fictitious particle creation lacks the capability of dealing with reflecting surfaces, white boundaries and periodic boundaries. The fictitious particles storage may overflow in the fictitious particles adjustment.
- 3) Only planar fictitious surfaces which are vertical to coordinate axes can be used.
- 4) The AIS method makes random number stride overrunning sometimes.
- 5) The calculation method of the estimated relative error is not precise enough.

Therefore, several novel improvements for the AIS method are described in this paper. Moreover, a coupled neutron-photon auto-Importance sampling method is proposed with the improved algorithms. In this new method, the variance reduction techniques of the AIS method can be applied to neutron and photon, simultaneously, in coupled neutron-photon Monte Carlo transport.

2 Materials and methods

2.1 Improved algorithms

2.1.1 Particle transport

In the AIS method, when the particle transport in each sub-space, except for the last sub-space, the particle will be killed once it traverses CFS, because its contributions to the current fictitious have been recorded by the fictitious particles. The particle position at each step of random walk will be checked to find whether it is in current or the next sub-space. Once the particle is located in the next sub-space, it will be killed. Although the fictitious particles can be created correctly in this way, the trajectory from CFS to the position where the particle is killed is recorded redundantly. This will affect the tally results around CFS, especially when mesh tally is used.

In the improved particle transport algorithm, after a source or collision event, the distance to CFS along the current direction will be calculated, and compared with the distance to the next geometry boundary and the next collision point. If the distance to CFS is the minimum, it will be the distance of the next random walk, and the particle will be killed on CFS.

As shown in Fig. 1, the particle will be killed at the next collision point A in the previous algorithm, and the trajectory t is redundant. In the improved algorithm, d will be the distance of the next random walk, and the particle will be killed at point B. Thus, it will ensure that the contributions to the whole geometry space are correct.

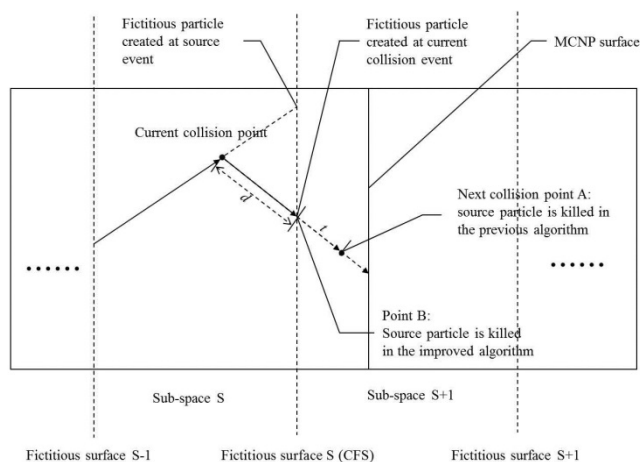


Fig.1. Improved particle transport algorithm

2.1.2 Fictitious particles creation and adjustment

In the AIS method, the fictitious particle weight is calculated by using next event estimator. The fictitious particle weight is equal to the probability that the particle has a collisionless free-flight to CFS along the current direction after a source or collision event. The AIS method does not support the reflecting surfaces, white boundaries and periodic boundaries, which leads to an underestimation of the fictitious particle weights and number. Actually, when the fictitious particle trajectory hits these surfaces or boundaries, its direction and location should be recalculated according to the type of the surface or boundary. Therefore, in the improved fictitious particles creation algorithm, the fictitious particle creation methods dealing with reflecting surfaces, white boundaries and periodic boundaries, are added to calculate the trajectory to CFS and the fictitious particle location.

As mentioned above, splitting/Russian roulette is used in fictitious particles adjustment. When the weight of the fictitious particle is higher than the mean weight, the particle is split and stored in the fictitious particles storage. If the number of fictitious particles is larger than the number of source particles, the mean weight will be recalculated and redundant particles will be eliminated. In the deep penetration problems with multiple materials, great changes may take place in the cross sections data between different materials, which will make the weights of the fictitious particles fluctuate remarkably. Additionally, when the small probability event that the source particle penetrates the shield is simulated, the weight of the resulting fictitious particle will be much higher than that of other fictitious particles, possibly many orders of magnitude higher. Hence, when the fictitious particles are split, a great number of “split fictitious particles” are generated, causing the fictitious particles storage overflow. Considering that the “split fictitious particles” have exactly the same particle state, there is no need to store all of them in the fictitious particles storage. In the improved fictitious particles adjustment algorithm, a single unit of storage space is set to store the state of “split fictitious particles”. Russian roulette is only performed on the serial numbers of fictitious particles, after which the fictitious particles are

re-extracted according to the serial numbers. In this way, the storage space is saved, and the data overflow is avoided.

2.1.3 Fictitious surface geometry

The whole geometry space is divided into several sub-spaces by fictitious surfaces in the AIS method. Only planar fictitious surfaces which are vertical to coordinate axes can be used. It cannot meet the demands in some deep penetration problems, for example, the reactor pressure vessel neutron fluence calculations, which require cylindrical fictitious surfaces to divide the reactor. Therefore, cylindrical and spherical fictitious surfaces are added to the AIS method. Furthermore, rotation and translation operations of fictitious surface are supported. RDUM card of MCNP is used as the interface of the fictitious surface parameter setting. The fictitious surfaces and the MCNP surfaces are independent of each other. As a consequence, the AIS method is applicable to the problem with more complex geometry.

2.1.4 Random number allocation

The Russian roulette used in fictitious particles adjustment will cause a large consumption of random numbers. MCNP uses correlated sampling that the i_{th} history will always start at the same point in the random number sequence. The value of the random number stride S allocated to each single history is only 152917 [10]. It cannot meet the demands of random numbers for fictitious particles adjustment, so that S is exceeded sometimes.

Two random number sequences are used in the improved random number allocation algorithm. The first random number sequence RS1 is the one used in MCNP. In an AIS simulation, K represents the number of fictitious surfaces and N_{src} represents the number of source particles from source region. Then, the number of histories that needs to be calculated is $(K+I) \times N_{src}$. Similar to MCNP simulation, the i^{th} history of the source particle from source region or fictitious surface, will always start at the same point in the random number sequence RS1. Thus, $(K+I) \times N_{src}$ random number strides will be used for an AIS simulation. RS1 is only responsible for the normal random walk to avoid exceeding random number stride. The second random number sequence RS2 is used only for

fictitious particles adjustment, and the initial random seed of RS2 is fixed. Different from MCNP simulation, RS2 is not segmented into many strides. Random numbers in RS2 are used one after another in an AIS simulation.

2.1.5 Calculation of the estimated relative error

The estimated relative error R at the 1σ level in the AIS method is defined as Eq. (1) and Eq. (2) [11].

$$R = \frac{S_{\bar{x}}}{\bar{x}}. \quad (1)$$

$$S_{\bar{x}} = \left(\sum_{k=1}^{K+1} \frac{S_k^2}{N_k} \right)^{1/2}. \quad (2)$$

Where \bar{x} is the estimated mean, $S_{\bar{x}}$ is the estimated standard deviation of the mean \bar{x} , N_k is the number of source particles in sub-space k which is equal to N_{src} in the AIS method, S_k is estimated standard deviation of the mean weight of fictitious particles created in sub-space k ($k=1,2,\dots,K$) or estimated standard deviation of the mean \bar{x} in the last sub-space.

The reason for using this error calculation method is that the AIS method uses layered particles transport model, and N_{src} source particles are transported in each sub-space. As a consequence, the contribution to the tally region of every single source particle from the source region cannot be obtained. However, this calculation method is not accurate. The states of the fictitious particles created on each fictitious surface are not able to accurately reflect the real distributions of weight, position, energy and angle; the error caused by particle elimination in fictitious particles adjustment is not recorded in S_k . Thus, in the improved algorithm of the estimated relative error calculation, the source particles are simulated by being divided into groups. N_{src} source particles are divided into m groups and m times of simulations are performed. In each simulation, N_{src}/m source particles are transported and the estimated mean of these N_{src}/m particles \bar{x}' can be calculated. Finally m samples of \bar{x}' are obtained, then the unbiased estimation of $S_{\bar{x}}$ is

$$S_{\bar{x}} = S_{\bar{x}'} / \sqrt{m}. \quad (3)$$

This algorithm is supposed to be more accurate since it accumulates all the transmission errors of the AIS method to the mean result of each group, avoiding

calculating the errors of each sub-space in the AIS method.

2.2 Coupled neutron-photon auto-importance sampling

In some radiation shielding designs, for instance, accelerator and reactor shielding, attenuation of neutrons and photons should be considered simultaneously. Accordingly, the deep penetration problems of coupled neutron-photon transport must be solved. In the AIS method, the variance reduction techniques can only be used for neutrons or photons, separately. The fictitious surface should only be used for the particles of the same type as the source particles. The particles of a different type from the source particles are transported normally, and the calculation efficiency of these particles is not increased. In order to solve this problem, we propose a coupled Neutron-Photon Auto-Importance Sampling (NP-AIS) method that can use the variance reduction techniques of the AIS method for both neutron and photon transport, simultaneously. The procedure of the NP-AIS method is as follows:

1) From source region to tally region, according to the shielding effect of the medium for neutron and photon, a series of neutron and photon fictitious surfaces are introduced to divide the whole geometry space into several sub-spaces. The total number of neutron and photon fictitious surfaces is K , and the number of sub-spaces is $K+1$. The fictitious surface k ($k=1,2,\dots,K$) is the CFS of sub-space k .

2) The Closest Photon Fictitious Surface (CPFS) and the Closest Neutron Fictitious Surface (CNFS) from the source are recorded.

3) The closest sub-space from the source is set to be current sub-space, in which the particles will be transported, and CFS is recorded. At least one of CPFS and CNFS is CFS. If CPFS and CNFS are at the same location, they are both set to be CFS.

4) The particles are transported from the source. At every source or collision events, fictitious particles are created on CPFS or CNFS using next event estimator according to the particle type.

5) When the source particle or secondary particle arrives at CFS, if the particle is neutron (or photon) and

CNFS (or CPFS) is CFS, the particle will be killed; if not, its state will be stored and transport will be stopped on CFS. It ensures that all the neutrons and photons will not traverse CFS.

6) After all the source particles are transported, the fictitious particles on CFS will be adjusted to be as many as the source particles using splitting/Russian roulette. These fictitious particles, source particles and secondary particles stored on CFS will be set as the source of the next sub-space. Then, the process will get back to step 1, and particle transport will be performed in the next sub-space.

When the closest fictitious surface of the same type as the particles is not CFS, the reason why the particles are stored and stopped on CFS in step 5 is shown in Fig. 2. If a neutron traverse CFS (CPFS) in sub-space S after collision event 1 and have collision event 2 which a secondary photon is generated, no photon fictitious particle will be created because the secondary photon is beyond CPFS. A neutron transport in the NP-AIS method is shown in Fig. 3.

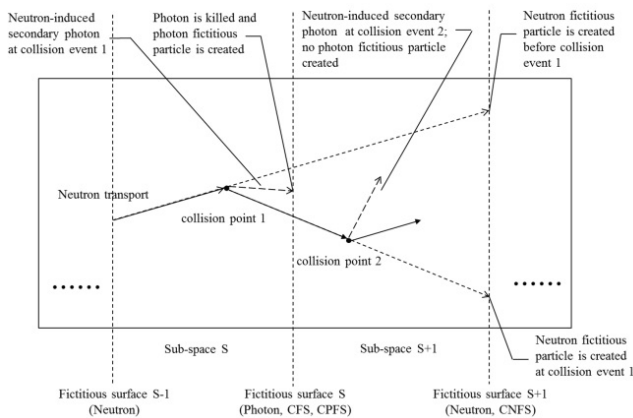


Fig.2. The situation when particle traversing CFS

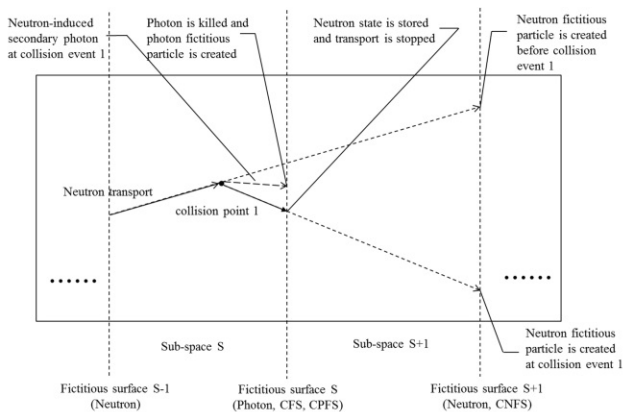


Fig.3. Particle transport in the NP-AIS method

Using these above variance reduction techniques of coupled neutron-photon transport and based on the improved AIS method presented in chapter 2.1, the NP-AIS method was implemented in MCNP5 Code.

2.3 Simulation set-up

In order to validate the reliability of the NP-AIS method, NUREG/CR-6115 PWR pressure vessel fluence calculation benchmark problems issued by the NRC [12] were calculated in this paper. The PWR model mainly consists of a 204 fuel assembly PWR core, a core barrel, thermal shield, vessel and an outer concrete biological shield. The detailed 15×15 fuel assembly pin-wise power distribution and the standard core loading pattern of the benchmark problems were used here. The azimuthal boundaries at 0 and 45 degrees were set to be reflecting boundaries. The outside of the biological shield wall, the top and bottom of the model were set to be void boundaries.

Five different examples including neutron/photon flux radial and axial distribution in biological shield wall, neutron/photon cavity flux ($E > 0.1$ MeV), neutron/photon flux spectrum at capsule location and neutron flux at pressure vessel 1/4 peak axial location ($E > 1.0$ MeV) were calculated by using MCNP5 code with the methods of NP-AIS, geometry splitting with Russian roulette (IMP-MC) and the analog Monte Carlo (A-MC), respectively. The geometry importance distribution of neutron was referred to the benchmark problem and the geometry importance distribution for photon was the same as that of neutron.

In NUREG/CR-6115 PWR benchmark, the thickness of biological shield wall made of concrete is 213.36 cm, while the biological shield wall used in the benchmark calculation in Ref. [12] was only 45.085 cm thick. No calculations inside or outside the biological shield wall were performed. In the first two examples, the whole 213.36 cm biological shield wall was added to the PWR model. In the latter three examples, in order to allow consistent comparisons with DORT results, the PWR model used was the same as that used in Ref. [12], in which the biological shield wall was 45.085 cm thick.

A figure of merit (FOM) was used to evaluate the computational efficiency. The FOM is defined as:

$$FOM = \frac{1}{R^2} \cdot T \quad (4)$$

All these calculations were performed on a notebook computer with Intel Core i7-3520M CPU 2.90 GHz and 16.0 GB memory.

3 Results and discussion

3.1 Neutron/photon flux radial distribution in biological shield wall

As shown in Fig. 4, 6 MCNP cylinder surfaces were added to biological shield wall. The fluxes of these 6 cylinder surfaces and the outer face of biological shield wall were tallied.

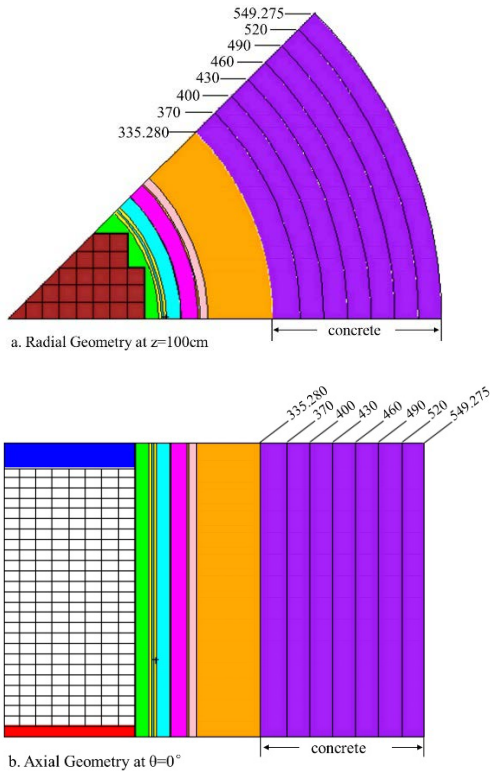


Fig.4. PWR model with full size biological shield wall (all dimensions in cm; the other parts of this model refer to Ref. [12]; color online)

In IMP-MC simulation, the number of the history (NPS) was 4×10^7 , and the computation time T was 4671 minutes.

In NP-AIS simulation, eleven neutron and eleven photon cylindrical fictitious surfaces whose radii were 188, 215, 230, 340, 360, 390, 420, 450, 480, 515 and 530 cm, were introduced. NPS was 10^5 and T was 11 minutes.

The neutron and photon results are shown in Table 1

and Table 2. R represents the estimated relative error. The neutron and photon FOM curves of IMP-MC and NP-AIS are shown in Fig. 5 and Fig. 6.

Table 1. Neutron flux radial distribution in biological shield wall

Surface No.	Radius (cm)	IMP-MC			NP-AIS		
		Flux per particle ($n/cm^2 \cdot s$)	R	FOM	Flux per particle ($n/cm^2 \cdot s$)	R	FOM
1	370	4.45E-10	0.002	95.15	4.57E-10	0.028	117.63
2	400	3.35E-11	0.003	19.66	3.42E-11	0.029	109.60
3	430	2.22E-12	0.011	1.68	2.21E-12	0.028	117.63
4	460	1.57E-13	0.042	0.12	1.44E-13	0.029	117.63
5	490	1.28E-14	0.156	0.01	9.86E-15	0.031	93.39
6	520	3.34E-16	0.488	0.00	6.97E-16	0.040	57.10
7	549.275	0	0	0.00	1.44E-17	0.056	28.68

Table 2. Photon flux radial distribution in biological shield wall

Surface No.	Radius (cm)	IMP-MC			NP-AIS		
		Flux per particle ($n/cm^2 \cdot s$)	R	FOM	Flux per particle ($n/cm^2 \cdot s$)	R	FOM
1	370	3.55E-10	0.002	83.63	3.48E-10	0.024	155.23
2	400	5.81E-11	0.003	27.31	5.66E-11	0.023	170.37
3	430	7.34E-12	0.007	4.91	7.46E-12	0.024	157.83
4	460	9.49E-13	0.018	0.70	9.01E-13	0.024	160.49
5	490	1.31E-13	0.043	0.11	1.21E-13	0.047	42.04
6	520	1.82E-14	0.119	0.02	1.60E-14	0.022	184.46
7	549.275	1.70E-15	0.163	0.01	1.63E-15	0.021	216.32

As shown in Table 1, for surface No. 1, 2, 3 and 4, the estimated relative errors of neutron results of IMP-MC and NP-AIS were all below 5%, and the neutron results of IMP-MC and NP-AIS were in good agreement. For surface No. 5, 6 and 7, IMP-MC could not give reliable results, whereas the estimated relative errors of neutron results of NP-AIS were still below 6%. As shown in Fig. 5, the neutron FOM curve of IMP-MC had an exponential decay with the surface radius increasing, because that the penetrating probability decreased through the concrete; however, the neutron FOM curve of NP-AIS kept stable approximately. The neutron FOMs of NP-AIS and IMP-MC for the first tally surface were almost equal, but the neutron FOM of NP-AIS for the last tally surface was increased by five orders of magnitude compared with that of IMP-MC. The similar performance for photon can be seen in Table 2 and Fig. 6. In this example, NP-AIS was much less time-consuming (only 11 minutes) than IMP-MC, but gave a much better performance.

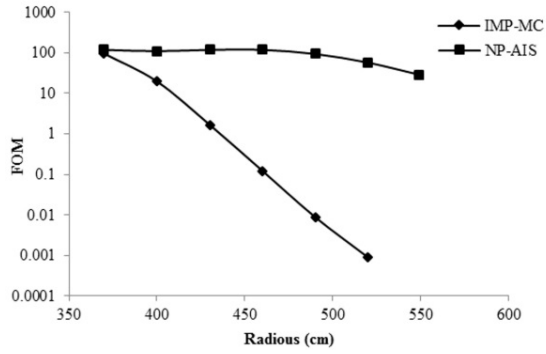


Fig. 5. FOM curves of neutron flux radial distribution in biological shield wall

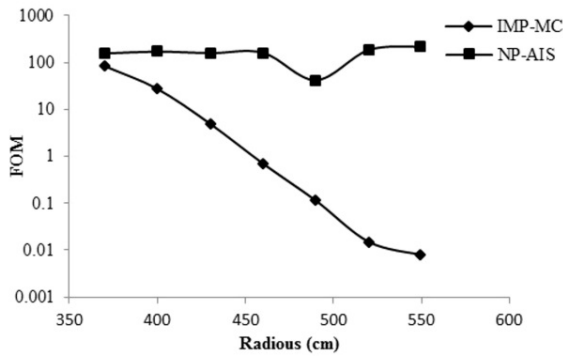


Fig. 6. FOM curves of photon flux radial distribution in biological shield wall

3.2 Neutron/photon flux axial distribution in biological shield wall

The same PWR model as example 3.1 was used. Considering the computational efficiency of IMP-MC, MCNP cylinder surface with radius of 490 cm was set to be the tally surface of neutron, and the MCNP cylinder surface with radius of 520 cm was set to be the tally surface of photon. The tally surfaces were divided axially into 13 segments at the z values of 30, 60, 90, 120, 150, 180, 210, 240, 270, 300, 330 and 360 cm. The flux of each surface segment was tallied.

In IMP-MC simulation, NPS was 4×10^7 , and T was 4776 minutes. The average estimated relative error of neutron was 47.76% and that of photon was 34.12%.

In NP-AIS simulation, NPS was 4×10^5 , and T was 43 minutes. The fictitious surfaces introduced were the same as those of example 3.1. The average estimated relative error of neutron was 4.08% and that of photon was 3.11%.

The results are shown in Fig. 7 and Fig. 8. The neutron and photon results of flux axial distribution in

biological shield wall of NP-AIS were very accurate. However, IMP-MC could not give reliable results even with unacceptable time-consumption.

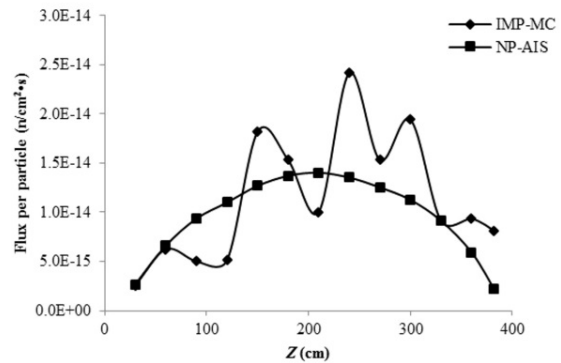


Fig. 7. Neutron flux axial distribution in biological shield wall

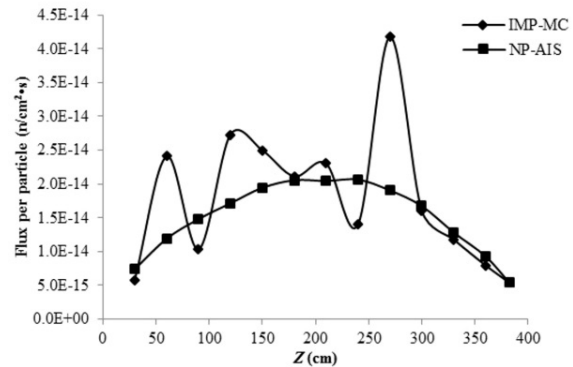


Fig. 8. Photon flux axial distribution in biological shield wall

The neutron and photon FOM curves of NP-AIS and IMP-MC for this example are shown in Fig. 9 and Fig. 10. The FOMs of NP-AIS were increased by about four orders of magnitude compared with those of IMP-MC for both neutron and photon. NP-AIS could give accurate results with reasonable time-consumption, whereas IMP-MC was not applicable to this example.

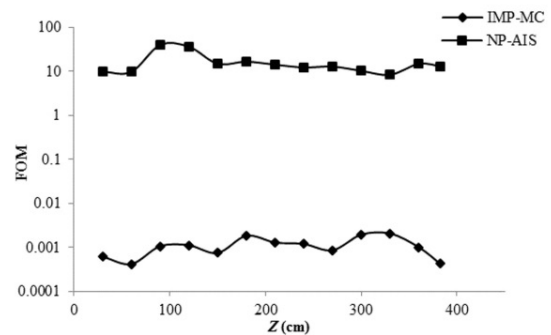


Fig. 9. FOM curves of neutron flux axial distribution in biological shield wall

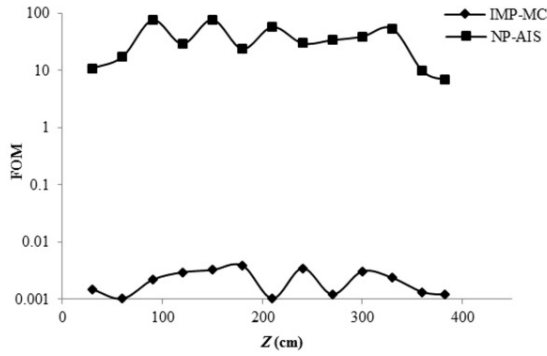


Fig.10. FOM curves of photon flux axial distribution in biological shield wall

3.3 Neutron/photon cavity flux ($E > 0.1$ MeV)

In this example and the following examples, because no photon calculations were performed in Ref. [12], the comparison with DORT or MCNP4A was only available for neutron results. The tally regions were located at $r=320.06$ cm and $z=177.27$ cm, and distributed uniformly over 61 azimuthal locations.

In IMP-MC simulation, NPS was 10^7 , and T was 1064 minutes. The average estimated relative error of neutron was 1.68% and that of photon was 2.83%.

In NP-AIS simulation, NPS was 5×10^6 , and T was 690 minutes. Four neutron and four photon cylindrical fictitious surfaces whose radii were 188, 215, 230 and 300 cm, were introduced. The average estimated relative error of neutron was 1.78% and that of photon was 2.41%.

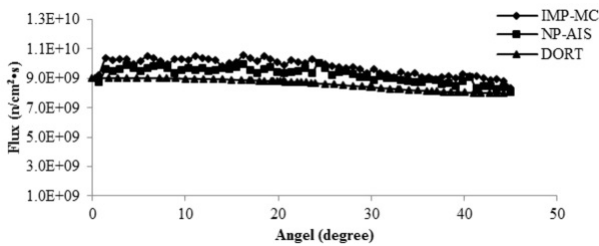


Fig.11. Neutron cavity flux ($E > 0.1$ MeV)

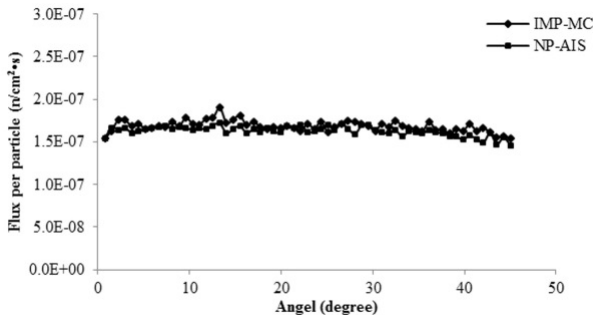


Fig.12. Photon cavity flux ($E > 0.1$ MeV)

The DORT results in Ref. [12], and the calculation

results of NP-AIS and IMP-MC, are shown in Fig. 11 and Fig. 12. The results of IMP-MC and NP-AIS were in good agreement. The average relative error of neutron compared between IMP-MC and NP-AIS was 5.19% and that of photon was 3.92%. Because of the different cross sections data and calculation methods of DORT, its results were lower than the results of IMP-MC and NP-AIS.

The neutron average FOM of IMP-MC was 3.21 and that of NP-AIS was 5.61. The photon average FOM of IMP-MC was 1.14 and that of NP-AIS was 2.90. In this example, computational efficiency increases of about two times were observed by using NP-AIS.

3.4 Neutron/photon flux spectrum at capsule location

The tally region was located at $r=320.06$ cm, $z=177.27$ cm and $\theta=9.5^\circ$, and the 47-group energy structure was used for spectrum tally, which were the same as the DORT calculations in Ref. [12]. NPS, the setting of fictitious surfaces and T were the same as those of example 3.3.

In neutron results of IMP-MC and NP-AIS, most of the estimated relative errors in the first 30 energy groups lower than 1.3534 MeV were below 10%, and that in the other high energy groups were all above 10%.

In photon results of IMP-MC and NP-AIS, most of the estimated relative errors in the energy groups from 0.11 MeV to 8.6 MeV were around 10%, and that in the other low and high energy groups were all above 10%.

The DORT results, and the calculation results of NP-AIS and IMP-MC, are shown in Fig. 13 and Fig. 14.

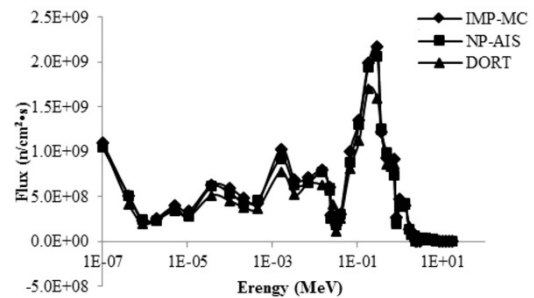


Fig.13. Neutron flux spectrum at capsule location

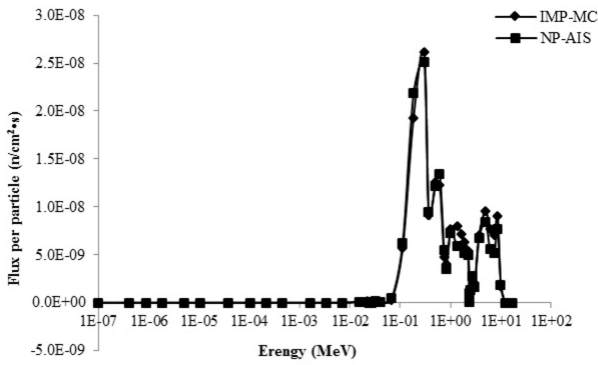


Fig. 14. Photon flux spectrum at capsule location

Referring to Fig. 13, although the neutron results of IMP-MC and NP-AIS were not very accurate, they were in very good agreement with the results of DORT, considering that DORT results should be lower than Monte Carlo results. Referring to Fig. 14, the photon results of NP-AIS were in good agreement with those of IMP-MC according to the estimated relative errors.

The neutron average FOM of IMP-MC was 0.18 and that of NP-AIS was 0.43. The photon average FOM of IMP-MC was 0.027 and that of NP-AIS was 0.073. In this example, computational efficiency increases of more than two times were observed by using NP-AIS.

3.5 Neutron flux at pressure vessel 1/4 peak axial location ($E > 1.0$ MeV)

The tally regions were located at $r=219.393$ cm and $z=125.488$ cm, and distributed uniformly over 20 azimuthal locations, which were the same as MCNP4A calculations in Ref. [12].

In IMP-MC simulation, NPS was 10^7 , and T was 870 minutes. The average estimated relative error of the results was 2.28%.

In NP-AIS simulation, NPS was 10^7 , and T was 515 minutes. Three neutron cylindrical fictitious surfaces whose radii were 188, 208 and 222 cm, were introduced. The average estimated relative error of the results was 3.67%.

In A-MC simulation, NPS was 10^9 , and T was 12107 minutes. The average estimated relative error of the results was 11.05%.

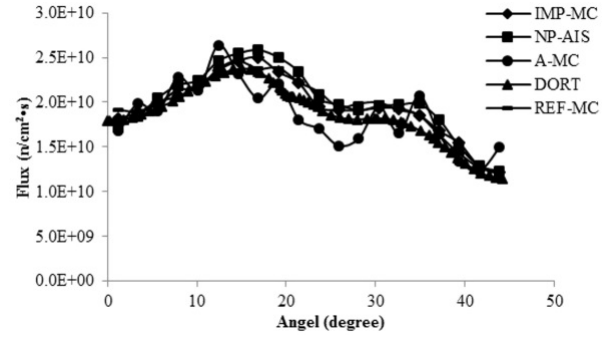


Fig. 15. Neutron flux at pressure vessel 1/4 peak axial location ($E > 1.0$ MeV)

The results of MCNP4A (REF-MC) and DORT in Ref. [12], and the calculation results of NP-AIS, A-MC and IMP-MC, are shown in Fig. 15. The results of REF-MC, IMP-MC and NP-AIS were in good agreement. The relative errors compared between NP-AIS and IMP-MC were from 0.16% to 7%, which were correct referring to their estimated relative errors. The average relative error compared between NP-AIS and IMP-MC was 3.72%, and that between NP-AIS and REF-MC was 4.56%. Accurate results could not be obtained using A-MC without any variance reduction techniques within an acceptable period of time.

The FOM curves of NP-AIS, IMP-MC and A-MC are shown in Fig. 16. The FOMs of NP-AIS and IMP-MC were both increased by more than two orders of magnitude compared with those of A-MC. There were 3 FOMs higher and 17 FOMs lower of NP-AIS than those of IMP-MC.

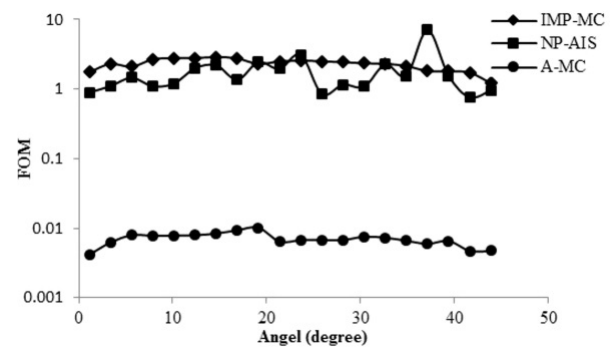


Fig. 16. FOM curves of neutron flux at pressure vessel 1/4 peak axial location ($E > 1.0$ MeV)

In this example, the performance of NP-AIS was slightly inferior to that of IMP-MC, because the penetrating probability of pressure vessel 1/4 peak axial location was not very low, and NP-AIS was designed to

solve deep penetration problems. Even though, NP-AIS could still give accurate results and produce very high computational efficiency.

4 Conclusions

In this paper, several improved algorithms for the AIS method are presented, and a coupled neutron-photon auto-importance sampling method is proposed. The NP-AIS method was validated by the NUREG/CR-6115 PWR pressure vessel fluence calculation benchmark. The results showed that NP-AIS method was applicable to different deep penetration problems, and improved the precision and efficiency of Monte Carlo method.

The computational efficiency of the NP-AIS method were much higher than that of geometry splitting with Russian roulette in all the examples, except for the neutron flux at pressure vessel 1/4 peak axial location example. In the neutron flux at pressure vessel 1/4 peak axial location example, compared with the analog Monte Carlo, the computational efficiency of the NP-AIS method was increased by about two orders of magnitude. Therefore, it can be deduced that the computational

efficiency of the NP-AIS method would be even higher than that of the analog Monte Carlo in other examples. Improvement of computational efficiency became more obvious when the penetrating probability decreased. In the examples of flux radial and axial distributions in biological shield wall, geometry splitting with Russian roulette was not able to give reliable results within an acceptable period of time, while the NP-AIS method could obtain very high calculation precision and efficiency. Furthermore, the NP-AIS method simultaneously improved the computational efficiencies of both neutron and photon.

According to the results analysis and the comparison above, the validity of NP-AIS method for complicated deep penetration problems of coupled neutron-photon transport is proved. The NP-AIS method can provide a reliable and efficient solution for deep penetration problems.

Reference

- 1 H. C. Gupta, *Ann. Nucl. Energ.*, 11(6): 283-288 (1984)
- 2 R. P. Gardner, M. Mickael, K. Verghese et al. *Nucl. Sci. & Eng.*, 98:1(1):51-63 (1988).
- 3 A. Haghghat, J. C. Wagner, *Prog. Nucl. Energ.*, 42(1): 25-53 (2003)
- 4 H. P. Smith, J. C. Wagner, *Nucl. Sci. & Eng.*, 149(1): 23-37 (2005)
- 5 L. J. Yuan, Y. X. Chen, J. R. Han, *At. Energ. Sci. & Technol.*, 48(3):407-411 (2014) (in Chinese)
- 6 W. T. Urban, T. J. Seed, D. J. Dudziak, *Nucleonic analysis of a preliminary design for the ETF neutral-beam-injector duct shielding*, in *4th Topical Meeting on the Technology of Controlled Nuclear Fusion*, (USA, 1981), p. 479
- 7 M. Kurosawa, *Radiat. Prot. Dosim.*, 116(1-4 Part2):513-517 (2005).
- 8 J. L. Li, C. Y. Li, Z. Wu, *Prog. Nucl. Sci. & Technol.*, 2: 732-737 (2011)
- 9 C. Y. Li, *Research of Point Flux Estimation and Deep Penetration in Monte Carlo Methods*, M.S. Thesis (Beijing, Tsinghua Univ. 2008) (in Chinese)
- 10 J. Tamsamani, T. Pederson, *MCNP-A General Monte Carlo N-Particle Transport Code, Version 5*. (Los Alamos National Laboratory, Oak Ridge, TN, 2003)
- 11 J. J. Fan, *Research of Rare but Important Events Simulation in Monte Carlo Methods*, Ph.D. Thesis (Beijing, Tsinghua Univ. 2004) (in Chinese)
- 12 J. F. Carew, *PWR and BWR pressure vessel fluence calculation benchmark problems and solutions*. (Division of Engineering Technology, Office of Nuclear Regulatory Research, US Nuclear Regulatory Commission, 2001)